Powder Technology 321 (2017) 94–104

Contents lists available at ScienceDirect

Powder Technology

journal homepage: www.elsevier.com/locate/powtec

Optimisation of blade type spreaders for powder bed preparation in Additive Manufacturing using DEM simulations

S. Haeri

Department of Mechanical and Aerospace Engineering, University of Strathclyde, Glasgow G1 1XJ, UK

ARTICLE INFO

Article history:
Received 6 May 2017
Received in revised form 24 July 2017
Accepted 6 August 2017
Available online 9 August 2017

Keywords:
Powder Bed Fusion
Additive Manufacturing
Discrete Element Method
Non-spherical particles
Multi-sphere approximation
Laser Sintering

ABSTRACT

Powders used in the Particle Bed Fusion process are spread onto compact layers and are then fused to generate a layer of the final part. This process is repeated layer-upon-layer to form the final product. It has recently been demonstrated (Haeri et al., 2017) that spreading the particles with a counter-rotating roller produces a bed with a higher quality (i.e. a lower void fraction) compared to a blade type spreader. This is related to the geometry of the two spreaders which directly changes the bed-spreader contact dynamic and consequently affects the bed's quality. Based on this rationale, here, it is postulated that changing the blade profile at the blade bed contact region can significantly enhance the bed's quality and improve the effectiveness of a blade as a spreading device. A set of Discrete Element Method (DEM) simulations is performed at device-scale to optimise the geometry of blade spreaders to yield the lowest void fraction using simple rod-shaped grains to control the computational costs. The blade profile is parametrised using a super-ellipse with three geometrical parameters. Firstly, it is demonstrated that geometric optimisation of a blade profile is an effective alternative to using more complex spreading devices. Secondly, for the proposed parametrisation, the optimum values are found using computer simulations and it is shown that bed volume fractions close to critical values are achievable. Finally, a new technique for multi-sphere approximation (MSA) is developed and applied to 3D models of real powder grains to generate realistic particle shapes for the DEM simulations. Then using these grains it is shown that the proposed optimum blade profile is capable of producing a bed with qualities comparable (and even better) to a roller at the actual operating conditions and with realistic grain characteristics.

1. Introduction

Powder Bed Fusion (PBF) is a promising Additive Manufacturing (AM) technology where polymeric or metallic particles, heated to just below their melting temperature are spread on a fabrication piston to form a thin powder bed (typically in the order of 0.1 mm) using a counter-rotating roller or a blade. Different technologies may then be used to fuse the material powder (see Fig. 1). For example, in a Laser Sintering (LS) process, a laser beam is used to fuse the powder grains. After this stage, the fabrication piston lowers the part slightly and a new layer of powder is applied. The process is repeated until the product is fabricated [1].

According to Gibson and Shi [2] one of the major parameters affecting the properties of manufactured parts by PBF is the material's behaviour and its characteristics during the processing while in a powder state. There are several studies focusing on effects of powder properties on the quality of parts. Shi et al. [3] suggested that the particle sizes between 75 and 100 μm are most suitable for PBF and in particular for Laser Sintering. Later, Goodridge et al. [4] suggested that parts made with a mixture of particle sizes have greater flexural strength due to a higher solid volume fraction (ϕ_s). The powder size distribution in relation to the laser power has also been investigated. For example, Hao et al. [5] suggest using higher laser energies for smaller particle sizes up to 50 μm.

More recently, Ziegelmeier et al. [6] focused on understanding the bulk and flow behaviour of polymer powders in relation to the properties of produced parts in LS. They mainly concluded that the tensile strength and elongation at break are enhanced by increasing ϕ_s. In addition, they examined the powder bed surface roughness and showed that at higher values, the part's surface roughness also increases. Berretta et al. [7] investigated the effects of particle characteristics (both grain and bulk), such as the size distribution, angle of repose, flowability and morphology on the quality of parts for poly ether ether ketone (PEEK) powder.

E-mail address: sina.haeri@strath.ac.uk.

http://dx.doi.org/10.1016/j.powtec.2017.08.011

Undoubtedly, the characteristics of individual particles have a significant effect on the success of PBF processes. Therefore, this fact cannot be ignored in any numerical technique used for design, prediction and understanding of PBF processes. The Discrete Element Method (DEM) is a particle based approach relying only on the first principles and is receiving significant attention recently for simulation of such systems. This is due to the capability of DEM to directly include the effects of grain characteristics such as material properties, size distribution and morphology. DEM was first proposed in late 1970s [8] and there is a large body of research on the method in geomechanics literature (see [9] for a modern introduction).

Application of DEM to PBF was pioneered by Zohdi [10–12] with regard to the development of laser heat sources and particle sintering models. Parteli and Pöschel [13] performed DEM simulations of the powder spreading process and found that the larger translational velocity of the roller and broader particle size distribution lead to a larger surface roughness. Xiang et al. [14], simplified the process by considering an assembly of 4000 particles undergoing three processes in their DEM simulations: random packing, layering and compression. They showed that the solid volume fraction increases by increasing the layer thickness. Steuben et al. [15] also proposed a new framework for modelling the full process including a laser heat source and powder sintering.

Haeri et al. [1] on the other hand provided DEM simulation of spreading process at *device scales* and used high ϕ_s and layer's surface roughness ϵ values as a measure of a successful powder spreading process (i.e. a high-quality bed). This is known to be directly correlated with the quality of final parts [6]. In their extensive parametric studies, Haeri et al. [1] investigated the effects of spreader type, its translational velocity, particle shape (and its distribution) and layer thickness on the bed quality. They parametrised elongated particles using their aspect ratios A_r and showed that the highest ϕ_s can be achieved at $A_r = 1.5$. They also analysed the micro-structures of elongated particles to explain the relation between various process parameters and the bed quality. They investigated two different types of spreading devices: rollers and blades. The consensus in the community is that the rollers generally produce higher quality powder beds which was confirmed in this study. Haeri et al. [1] however, related this to a particle dragging phenomenon and a small contact area between a blade spreader and the bed.

In this paper, it is postulated that since a low-quality bed generated using a blade is essentially a result of its geometry – as was suggested in [1] – it can be rectified purely by geometric modification of the blade. Therefore, a new class of blades is proposed with a modified head profile. The suggested profile is a supper-ellipse with three adjustable parameters. It is shown that simple geometrical modifications can significantly affect the bed quality and then using a series of computer simulations the best values for the these parameters are identified and reported. The optimised profile is then compared with a roller type spreader at different operating conditions and for realistic particle shapes. The powder grains are approximated using a new multi-sphere approximation (MSA) technique which will be discussed in detail. It is then shown that the optimised profile is capable of generating a powder bed with qualities (in terms of ϕ_s) on par with those generated using a roller at different operating conditions and with realistic grain shapes. This could greatly reduce the production and maintenance costs of the PBF devices by obviating the need for significantly more expensive and complex spreading devices.

2. Methodology

2.1. Discrete Element Method

The Large-scale atomic/molecular massively parallel simulator (LAMMPS) code [16] is used for all the DEM simulations. A linear Hookean spring-dashpot contact force model is applied to each pair

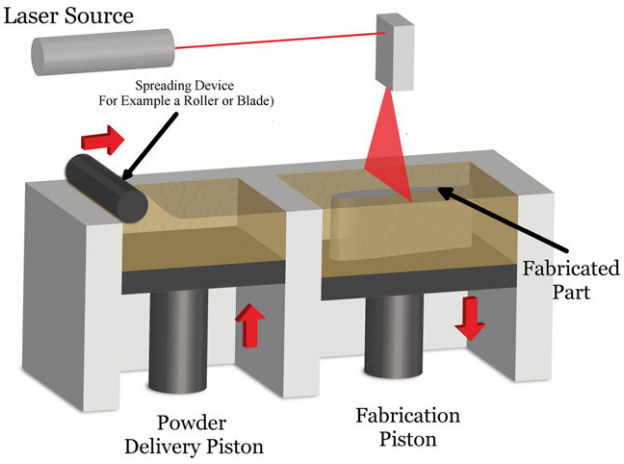

Fig. 1. Schematic presentation of the Laser Sintering process.

of particles p and q whenever the two particles overlap, i.e. when $\delta_{pq} = R_p + R_q - r_{pq} > 0$, where $r_{pq} = \|\mathbf{r}_p - \mathbf{r}_q\|$, and $\|\cdot\|$ represents the Euclidean norm (magnitude) of any vector. In addition, R_k, $k \in \{p, q\}$, is the radius of the kth spheroid and $\mathbf{r}_k$ is the position vector of its centre of mass (CoM). The normal and tangential components of spring-dashpot force are given by

$$\mathbf{F}^n = \kappa_n \delta_{pq} \mathbf{n}_{pq} - \gamma_n m^* \mathbf{v}^n_{pq} \tag{1}$$

$$\mathbf{F}^t = -\kappa_t \mathbf{u}^t_{pq} - \gamma_t m^* \mathbf{v}^t_{pq}, \tag{2}$$

where $\kappa_n, \gamma_n, \kappa_t$ and γ_t are spring elastic and damping constants in normal and tangential directions respectively. In addition, $\mathbf{v}^n_{pq}$ and $\mathbf{v}^t_{pq}$ are relative normal and tangential velocities. The effective mass is defined as $m^* = m_p m_q/(m_p + m_q)$ where m_k, $k \in \{p, q\}$, is the mass of kth particle. The unit normal vector in the direction of the line connecting a pair of spheroid centres is presented by $\mathbf{n}_{pq}$ and elastic shear displacement by $\mathbf{u}^t_{pq}$. The tangential force is limited to $\left\|\mathbf{F}^t_{pq}\right\| \le \mu_c \left\|\mathbf{F}^n_{pq}\right\|$ where μ_c is the Coulomb friction coefficient which is set to 0.5 in this study [1] considering the angle of repose test results for different PEEK powders reported by Wang et al. [17]. Similarly, a normal $\mathbf{F}^n_{pw}$ and a tangential force $\mathbf{F}^t_{pw}$ are defined between particle p and the bottom wall w.

Shape effects are considered in this paper and hence, a versatile multi-sphere technique is used [1]. The DEM, as described above, is formulated for sphere-sphere collisions. In the multi-sphere approach, the contacts are still detected between sphere pairs. However, instead of integrating the Newton's laws of motion for each sphere, a total force and torque around the CoM of each non-spherical particle is calculated by adding-up individual contact forces of its constituent spheres. The CoM position of each rod is then updated using Newton's laws of motion and the location of individual spheres is updated assuming rigid-body dynamics.

In this paper, initially rod-shaped particles are considered which can be parametrised using an aspect ratio A_r. This is chosen since elongated particles with a similar aspect ratio distribution and round edges can be considered as crude approximations to a population of impact-milled PEEK particles [1]. In addition, rod-shaped particles with required aspect ratios of $A_r = 1.5$, 2.0, and 2.5 could be generated with 2, 3 and 4 spheroids, considerably reducing the computational costs. Therefore, these are used as crude approximations

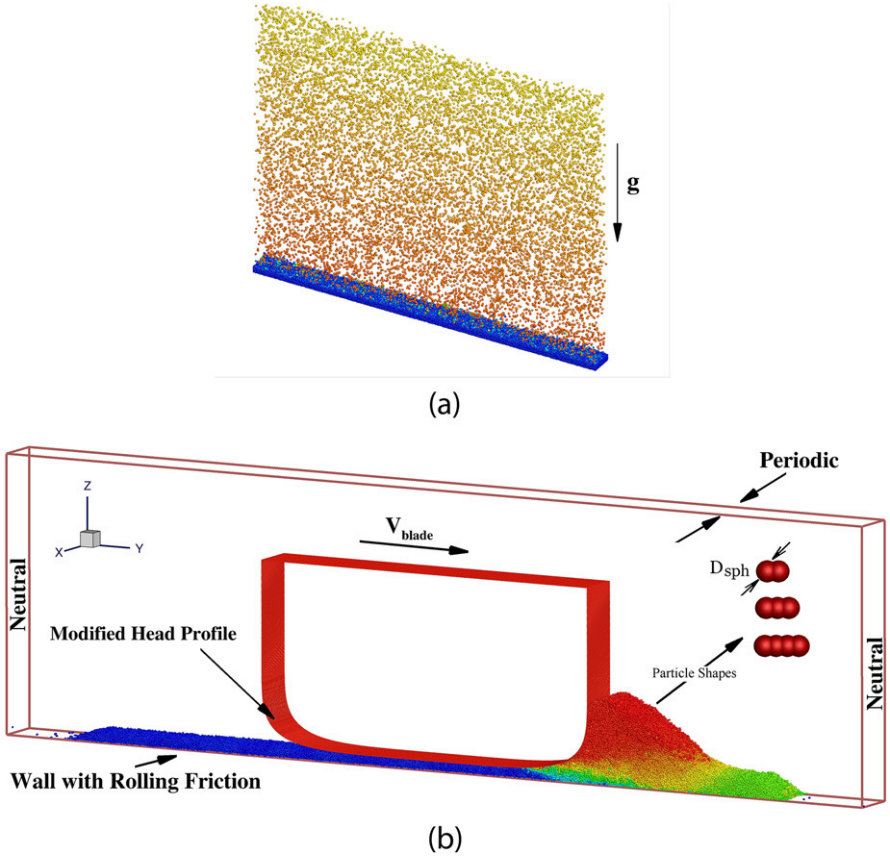

Fig. 2. The device simulation set-up and initial preparations presented for a modified blade profile. (a) The initial bed preparation using a rain fall technique is presented; particles are coloured with their velocity magnitudes and diameters are not to scale for better presentation. (b) The rod-shaped particles with different aspect ratios A_r are presented using a multi-sphere approach. Also, the particles are coloured in a representative simulation with v_y (velocity in y-direction). Only a section of the spreader with a width L_x is simulated by choosing periodic boundary conditions in x-direction and in y-direction neutral walls are used (no interaction with particles).

to the real particles, for the first stage of optimisation where a large number of simulations is required.

An initial assembly of particles (before the spreading) is created using a rainfall technique (Fig. 2a). Also, the simulation set-up is depicted in Fig. 2b. The bottom boundary is a rigid wall that exerts a normal and a tangential force on the particles (equivalent to assuming an infinity large sphere in Eqs. (1) and (2)). To prevent unbounded rotation of particles on the bottom wall, a rolling friction model is implemented. The adopted model constantly applies a resistive torque to the particles in contact with the bottom wall, which is given by [18–20]

$$\mathbf{T}_{pw} = -\mu_r R_p \left\| \mathbf{F}_{pw}^{n} \right\| \frac{\boldsymbol{\omega}^{\mathrm{rel}}}{\left\| \boldsymbol{\omega}^{\mathrm{rel}} \right\|}. \tag{3}$$

In Eq. (3) ω_i^{rel} is the relative angular velocity between particle p and the bottom wall w and $\mu_r = 0.005$ is used for all the simulations based on the analysis of Zhou et al. [18] and Haeri et al. [1]. The elastic spring constant κ_n, in Eq. (1) is set according to [21]

$$\kappa_n = \frac{16}{15}\sqrt{R^*}Y^*\left(\frac{15m^*V_c^2}{16\sqrt{R^*}Y^*}\right)^{\frac{1}{5}}, \tag{4}$$

and the dash-pot constant is calculated as

$$\gamma_n = \sqrt{\frac{4\kappa_n(\ln E)^2}{m^*\left[\pi^2 + (\ln E)^2\right]}}, \tag{5}$$

where $1/R^* = 1/R_p + 1/R_q$, $1/m^* = 1/m_p + 1/m_q$, $1/Y^* = \left(1-\nu_p^2\right)/Y_p + \left(1-\nu_q^2\right)/Y_q$. In addition, Y, E, ν and V_c are the Young's modulus, coefficient of restitution, Poisson ratio and a characteristic velocity respectively. The coefficient of restitution is set to 0.5. The values of Young's modulus and Poisson ratio are set to 3.7 GPa and 0.4 for all particles which are typical values for PEEK polymeric particles [22]. Assuming $V_c = V_{\mathrm{blade}}^T$ $\left(\text{or } V_{\mathrm{spreader}}^T\right)$, Eq. (4), yields $\kappa_n \approx 1500\mathrm{N/m}$ depending on the roller velocity. Therefore, a constant value of $\kappa_n = 1500$ is adopted for all the simulations. The tangential force constants κ_t and γ_t are respectively set to $2/7\kappa_n$ and $1/2\gamma_n$ (see Shäfer et al. [23] for details).

The spring-dashpot model is chosen in this study due to its low computational costs. Despite the simplicity of the model, Di Renzo and Di Maio [21] showed that if the parameters of the model are accurately chosen, the model performs as well as the full Hertz-Mindlin and Deresiewicz model – and better than the simpler versions of this model – as long as the details of collision forces are not relevant (for example in particle breakage). It is also worth mentioning that, absolute values for the parameters measured in this paper may vary depending on the powder physical properties, shape and size distribution among other factors. Nevertheless, the new designs are expected to remain effective for metallic/polymeric powders used in AM. In this study the blade design to maximise volume fraction is of interest and the trends are used to guide the design. Therefore, absolute values – which will be affected by the aforementioned factors – have no impact on the validity of the conclusion drawn here.

Table 1
A summary of simulation and post-processing parameters with a short description. This is provided for reference only and the parameters are explained in detail in the text. In addition, all the dimensional parameters are reported in SI units.

Parameter	Description	Value
m^*	Effective mass for particles "p" and "q"	$m^* = \frac{m_p m_q}{m_p+m_q}$
κ_n	Normal spring constant [1]	1500
E	Coefficient of restitution	0.5
μ_c	Coulomb friction coefficient	0.5
γ_n	Normal dash-pot constant	$\sqrt{\frac{4\kappa_n(\ln E)^2}{m^*[\pi^2+(\ln E)^2]}}$
κ_t	Tangential spring constant [23]	$2/7\kappa_n$
γ_t	Tangential dash-pot constant [23]	$1/2\gamma_n$
μ_r	Rolling friction constant Haeri et al. [1]	0.005
D_{sph}	Sphere diameter (for rods)	10^{-4}
ρ_{rod}	Particle density (PEEK)	1300
ℓ	Sphere overlap	$0.5D_{\text{sph}}$text
A_r	Aspect ratio	$\in \{1.0, 1.5, 2.0, 2.5\}$
L_x, L_y, L_z	Domain size in x, y, z	$2.46 \times 10^{-3}, 0.04, 0.03$
δ_{init}	Layer thickness (before spreading)	$10D_{\text{sph}}$
δ_{spreader}	Spreader's displacement	$5D_{\text{sph}}$
a_s	Spreader profile thickness parameter	$(10, 25, 100)D_{\text{sph}}$
b_s	Spreader profile hight parameter	$(10, 20, 50)D_{\text{sph}}$
n_s	Spreader profile shape parameter	$(0.5, 1.0, 1.5, 2.0, 5.0)$

2.2. Simulation set-up and post-processing

The rods with various aspect ratios $A_r = 1.5, 2.0, 2.5$ are created by overlapping spheres with an overlap of $\ell = 0.5D_{\text{sph}}$ (Fig. 2b) and number densities of $N_{A_r} = 0.5, 0.3, 0.2$ respectively. The initial configuration (before the spreading starts) is prepared by pouring randomly generated particles on the bottom wall (see Fig. 2a). This is done within a simulation box with dimensions $L_x = 2.46 \times 10^{-3}$, $L_y = 0.04$ and $L_z = 0.03$. The geometric parameters L_x, L_y and L_z are the width, length and height of the simulation box (red boundaries in Fig. 2b). Note that all values are in SI units except otherwise stated. The preparation method is different from the delivery system in LS devices; nevertheless, since the powder is not compacted in the delivery piston and rests under its natural weight, this method of initiating the simulation, is adequate for the current purpose.

The box size in the flow-direction L_y changes to accommodate all the particles as they are spread and the corresponding walls exert no force on the particles (walls labelled neutral in Fig. 2b). The number of particles in each simulation is adjusted to supply an initial thickness of $\delta_{init} \approx 10D_{\text{sph}}$ for all particle types, where D_{sph} is the diameter of spheres used to generate the rod-shaped particles. In addition, the blade displacement from the bottom wall, δ_{blade} is set to $5D_{\text{sph}}$ which is the profile's minimum distance to the bottom wall and essentially sets the powder bed thickness. Table 1 summarises all the parameters used in this study.

The solid volume fraction, ϕ_s, is calculated and its maximum value is used as the objective function – which means a more effective spreading process – to optimise the blade profile. The ϕ_s values are calculated using a Voronoi tessellation technique [24] and only a section of the bed away from the edges are considered to suppresses the end effects; this is achieved by only including the particles in the calculations that fit within the bounding box away from both ends and the bed's surface. The details of choosing this box, in addition to sensitivity of the results on this choice are discussed in great details in Haeri et al. [1]. This is, in fact, a reasonable assumption since the full extent of the bed in not normally used for fabrication.

3. The new blade design

Haeri et al. [1] argued that an "effective" bed-spreader contact, determines the quality of a prepared powder bed (a high ϕ_s and low ϵ). Based on visualisations of the bed-spreader contact dynamics they related this to a particle dragging phenomenon which distorts the bed if a spreader type did not provide an effective support for the particle heap that forms in front of the spreader (see Fig. 2b). This suggests that a geometric modification of the spreader should in principle, significantly improve the bed's quality.

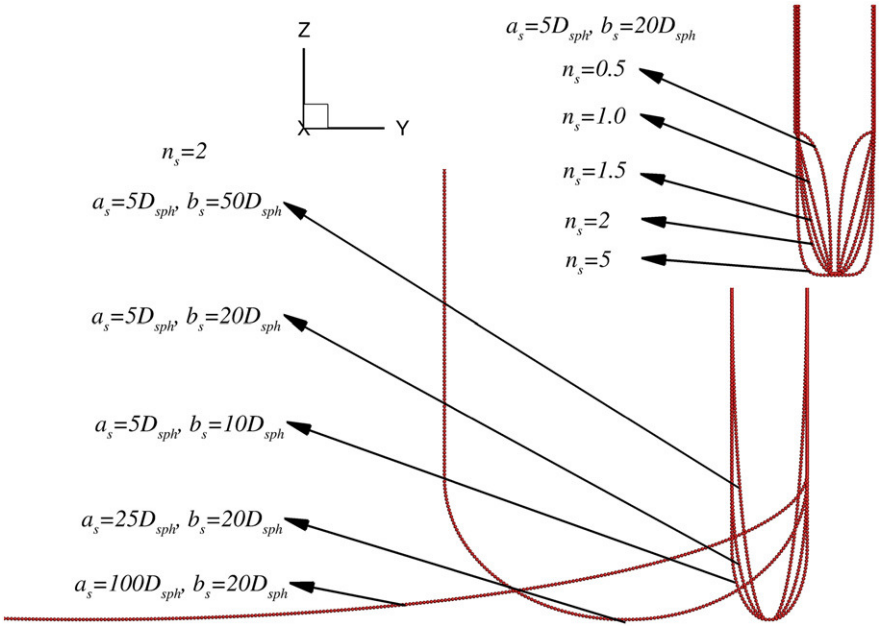

Fig. 3. Different spreader profiles used for the optimisation. Only a subset of all designs are presented to show the effects of changing parameters a_s, b_s and n_s. Only half of the widest blade with $a_s = 100D_{\text{sph}}$ is presented.

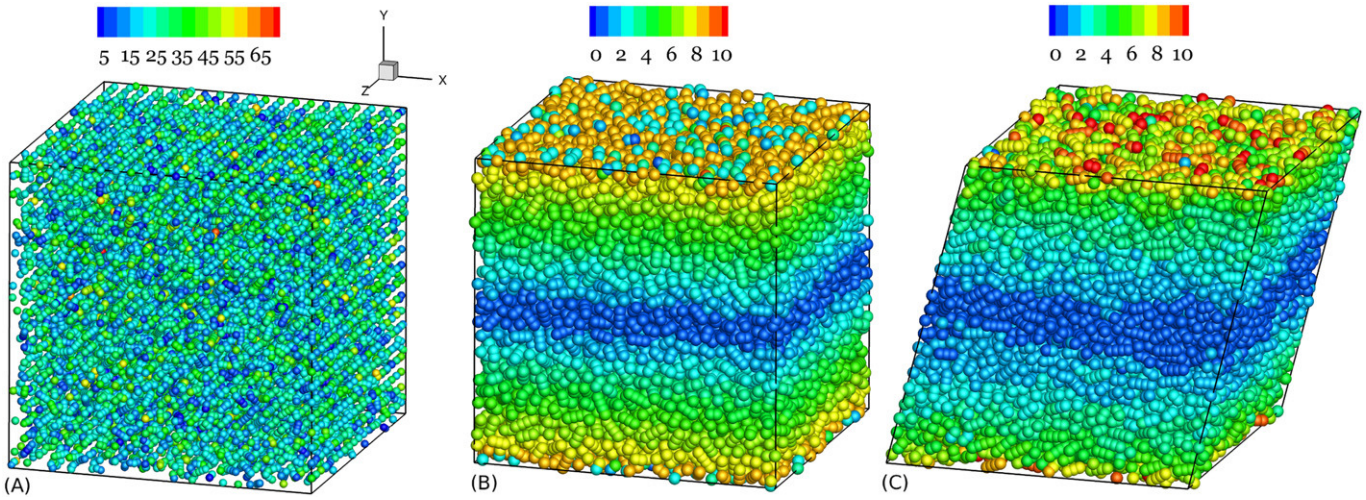

Fig. 4. Simple shear flow simulation of rod-shaped particle assembly with $A_r = 1.5, 2.0, 2.5$ and number densities $N_{A_r} = 0.5, 0.3, 0.2$. (A) The initial configuration before compression to the desired volume fraction. (B) The configuration after homogeneous compression to the desired volume fraction (presented for $\phi = 0.57$). (C) Sheared assembly. Note that figure (A) is scaled differently compared to (B) and (C). Particles are coloured with their velocity magnitudes.

By modifying the spreader's head profile a new class of spreading devices is suggested. A super-elliptic profile with three parameters n_s, a_s and b_s is proposed here:

$$\left|\frac{y}{a_s}\right|^{n_s} + \left|\frac{z}{b_s}\right|^{n_s} = 1. \tag{6}$$

The parameters n_s, a_s and b_s respectively, control the overall shape, width and height of the profile. The blade thickness is $w_s = 2a_s$ and its height is $h_s \gg b_s$. Note that the blade's height is longer than b_s and remains a straight line for $z > b_s + \delta_{\text{blade}}$, its value is chosen to be larger than the maximum height of the powder heap formed in front of the blade during the spreading process and has no effect on the optimisation results. In Fig. 3 various profile shapes proposed for the optimisation are presented. Three values $(10, 25, 100)D_{\text{sph}}$ and $(10, 20, 50)D_{\text{sph}}$ are chosen for a_s and b_s respectively. The parameter n_s determines the overall shape of the profile. Initially, five different shapes $n_s \in \{0.5, 1.0, 1.5, 2.0, 5.0\}$ are considered (see Fig. 3), however, after the initial optimisation a few more values are considered to show that the best value identified is in fact the optimum value.

3.1. The particle assembly characteristics

Before starting the main computer experiments, it is necessary to acquire a better insight into the jamming behaviour of an assembly of particles with a similar distribution of A_r. This will allow to set reasonable objectives for the new blade designs. The critical volume fraction ϕ_s^c – where the jamming transition occurs – is selected as the objective. To achieve $\phi_s > \phi_s^c$, significant compressive forces are required which may be achieved by a subsequent compression. However, this increases the process complications and significantly slows down the fabrication and is not a normal practice. Alternatively, it could be accomplished by reducing the displacement between previous layer and the spreader. This, however, could adversely affect the volume fraction due to particle jamming [1] particularly for elongated particles. Therefore, a volume fraction close to ϕ_s^c seems to be a reasonable expectation.

To understand the jamming behaviour of the assembly considered for computer experiments, see Section 2.2, a set of simple shear flow simulations are performed. For all the simulations an initial assembly is prepared by producing a non-overlapping lattice of $N_p = 20 \times 20 \times 20 = 8000$ particles, initializing each particle velocity and orientation to a random value – Fig. 4 – followed by homogeneous compression to the desired volume fraction ϕ in a periodic box with Lees-Edwards boundary conditions [25]. After, shearing the assembly, see Fig. 4, the stress is calculated by adding contributions from collision and velocity fluctuations:

$$\boldsymbol{\sigma} = \frac{1}{V}\left[\sum_{p=1}^{N_p}\sum_{\substack{q=1\\q\neq p}}^{N_p} \mathbf{r}_{pq}\mathbf{F}^c_{pq} + \sum_{p=1}^{N_p} m_p \mathbf{v}'_p \mathbf{v}'_p\right], \tag{7}$$

where V is the volume of the simulation box and $\mathbf{v}'_p$ is the fluctuating velocity component of pth particle. The pressure – mean normal stress – is then given by $P = (\sigma_{11} + \sigma_{22} + \sigma_{33})/3$ and the relevant stress component is $\sigma_{12} = \sigma_{xy}$. All the collision model parameters

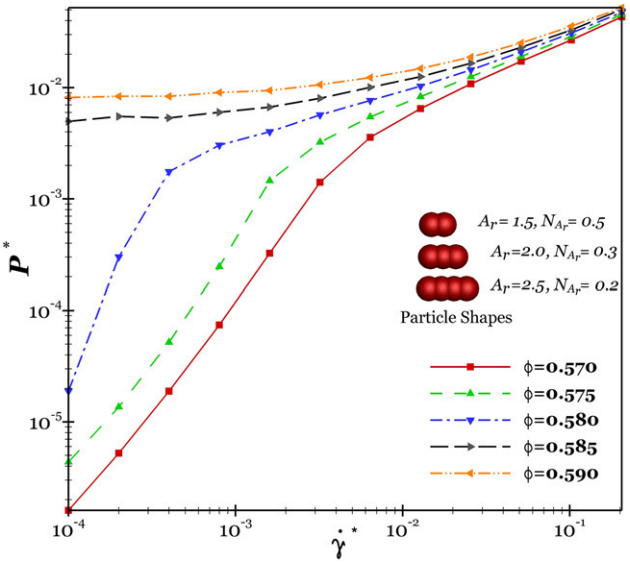

Fig. 5. Determination of the critical volume fraction for the assembly of particles shown on the figure. Non-dimensional flow curves are presented at various volume fractions and shear rates to identify $\phi_s^c = 0.58$.

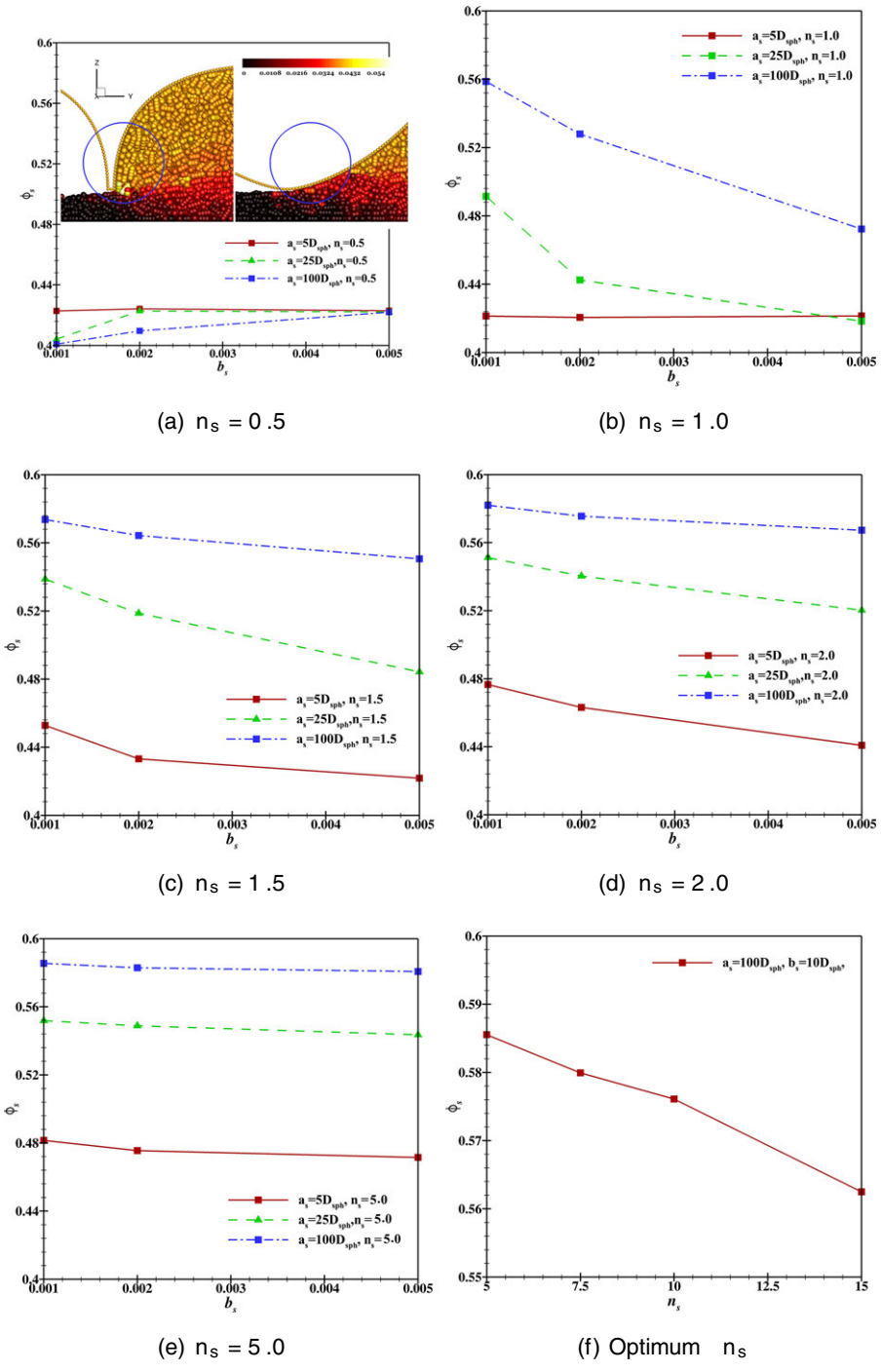

Fig. 6. Variations in solid volume fraction ϕ_s with different optimisation parameters. The values on b_s axis correspond to $(10, 20, 50) \times D_{\text{sph}}$. In the inset of figure (a), the velocity magnitude of particles near two blades with $n_s = 0.5$ and 1.5, with $a_s = 25D_{\text{sph}}$ and $b_s = 20D_{\text{sph}}$ are highlighted.

are set to those used for the device scale computer simulations. It is well established [26,27] that the flow curves (e.g. P vs $\dot{\gamma}$, where $\dot{\gamma}$ is the shear rate) for dry granular material exhibit a drastic jump by increasing ϕ_s to values above ϕ_s^c. Therefore, generating a few flow curves proves to be a convenient and fast technique to identify the ϕ_s^c. Fig. 5 shows the results of 60 simulations. In this figure $P^* = PD_{eqv}/\kappa_n$ versus $\dot{\gamma}^* = \dot{\gamma}D_{eqv}/\sqrt{\kappa_n/(\rho_s D_{eqv})}$ are presented. Here, D_{eqv} is defined by $\sum_i N_{A_r,i} D_{eqv}^i$ and D_{eqv}^i is the equivalent diameter of particles with an specific $A_r \in \{1.5, 2.0, 2.5\}$.

Clearly, the critical volume fraction happens between $\phi_s = 0.575$ and $\phi_s = 0.585$. The curve for $\phi_s = 0.580$ shows the typical behaviour very close to the ϕ_s^c such as very large fluctuations and difficult convergence at low $\dot{\gamma}$. For $\dot{\gamma}^* \geq 4 \times 10^{-4}$ the curve for ϕ_s^c continues on the asymptote to the quasi-static and inertial regimes. The erratic behaviour of the curve for $\dot{\gamma}^* \leq 4 \times 10^{-4}$ is a direct indication of very large variances in the stress calculations which require extremely long simulation to statistically converge. It is possible to subdivide the interval between $\phi_s = 0.580$ and $\phi_s = 0.585$ and run the simulations for longer to obtain a more accurate estimate. However, the current accuracy is sufficient for our purpose and $\phi_s = 0.58$ is identified as the critical volume fraction for the assembly of particles under consideration.

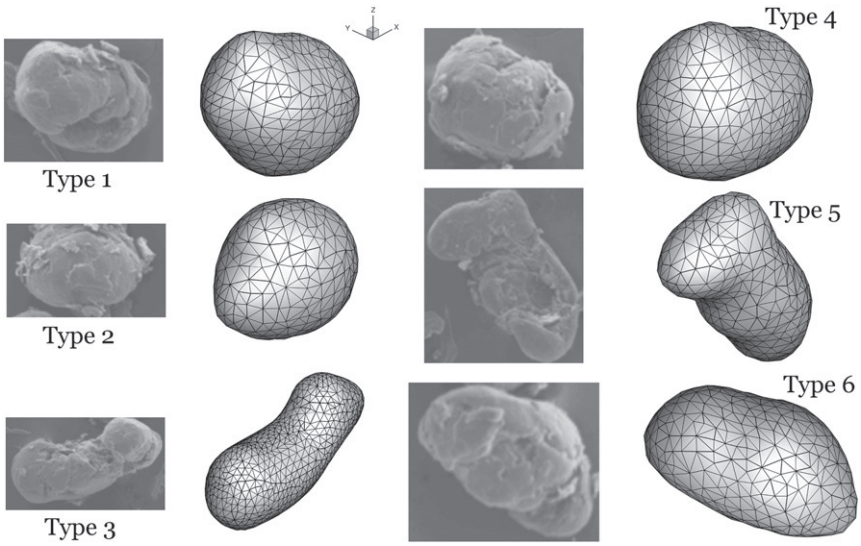

Fig. 7. 3D reconstruction of realistic PEEK particles. Images of the impact-milled particles are extracted from a Scanning Electron Microscope (SEM) image of a sample of the powder which are presented alongside the corresponding 3D reconstructed stereo-lithography (STL) models. The image data are taken from the publicly available data-set by Haeri [29].

3.2. Optimisation results and discussions

The results of 48 simulations with different optimisation parameters are presented in Fig. 6. Before analysing the results any further, it is clear that the blade's geometry is indeed a major parameter for controlling the bed quality. Fig. 6 clearly shows the variation in ϕ_s from low values of $\phi_s \approx 0.4$ to values as high as $\phi_s \approx 0.58$ close to the critical volume fraction for elongated particles. This proves the effectiveness of geometrical modification of the blade's head profile to maximise ϕ_s and indicates the validity of the initial hypothesis.

For comparison with a straight edge blade, the data from [1] are used. They performed simulations with mono-sized ($A_r = 1.0 \cdots 2.5$) particles at similar operating conditions. However, they showed that the characteristics of poly-sized beds (with small variation in the aspect ratios) could be approximated by a number density weighted averaging. To find an approximate value for the poly-sized case considered here, a number density average of the mono-sized simulations of [1] is calculated. This can be written by $\phi_s = \sum N_i \phi_s(A_{r,i})$ which yields a value of $\phi_s = 0.4$ for straight edge blade spreader of a mixture of particles with number densities considered in this paper. The effects of overall profile shape are demonstrated in Fig. 6a–e. In these figures, the value of the parameter n_s is changed which characterises the overall shape of the profile. A value of $n_s = 0.5$ generates a concave profile and the results are presented in Fig. 6a. Evidently, this profile does not improve the compaction significantly, nevertheless, some improvement is observed especially for the lowest value of blade width of $5D_{sph}$.

A linear profile can be generated by setting $n_s = 1$. The simulation results for this profile and different width and height parameters a_s and b_s are presented in Fig. 6b. The bed quality – as expected – is a function of both profile height and also the spreader width. Generally, shorter (smaller b_s) and wider (larger a_s) profiles generate higher volume fractions ϕ_s. The sensitivity of the linear profile to height is higher for wider designs but almost no dependence on height is observed for narrow designs ($a_s = 5D_{sph}$). It is also interesting to note that ϕ_s dependence on a_s for the concave profile ($n_s = 0.5$) is opposite to that of the linear profile and all the other convex profiles. It is believed that for a concave profile ($n_s = 0.5$) some particles may get clogged in the hollow region between the blade's head profile and the bottom surface (or the previous layers).

The region close to the head is highlighted in the inset of Fig. 6a. It is clear that the particle velocities for the presented convex profile ($n_s = 1.5$) increase gradually from zero at bed-blade minimum contact point (i.e. the point on the blade with minimum z) to V^T_{blade}; whereas for the concave profile ($n_s = 0.5$) there is sudden change in the velocities close to the blade. This indicates the clogging of powder grains which eventually degrades the bed. This effect is exaggerated as the hollow region width is increased since more particles are

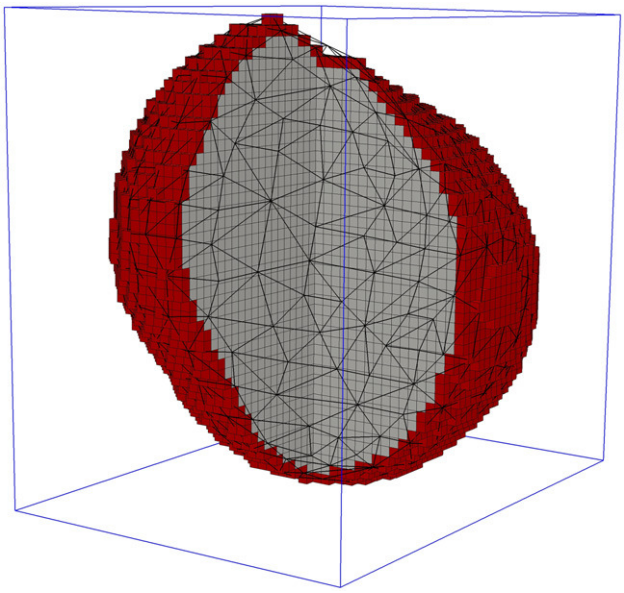

Fig. 8. Discretization of the STL object using stair-step cells. The surface cells are coloured in red and internal cells in grey. The black triangulation is the surface presentation of the original STL and the bounding box presented with blue edges for Type 1 particle (see Fig. 7). The reader is referred to the online version of the figure if the colours are not clear in print.

Table 2
Accuracy of the stair-step discretization of the particle's STL. The relative error in particle volume is calculated with respect to the analytical value given by Eq. (10). The relative 2-norm and ∞-norm errors in $\mathbf{I}_p$ are calculated with respect to the $\mathbf{I}_p^{MC}$ which is calculated using a standard Monte Carlo integration technique.

Particle type	$\frac{\lvert V_p^{STL}-V_p\rvert}{V_p^{STL}} \times 10^4$	$\frac{\lVert \mathbf{I}_p-\mathbf{I}_p^{MC}\rVert_2}{\lVert \mathbf{I}_p^{MC}\rVert_2} \times 10^3$	$\frac{\lVert \mathbf{I}_p-\mathbf{I}_p^{MC}\rVert_\infty}{\lVert \mathbf{I}_p^{MC}\rVert_\infty} \times 10^3$
1	0.7133	2.8821	3.9983
2	8.7765	5.3901	6.6475
3	14.676	2.7746	3.3642
4	6.3613	4.3804	5.3872
5	0.8422	2.9625	3.1482
6	2.0593	0.9668	1.1357

trapped in the larger hollow space. Therefore, wider profiles generate smaller volume fraction for the $n_s = 0.5$ case whereas increasing a_s improves the quality for all other convex profiles (with $n_s \geq 1$).

Panels c–e in Fig. 6 show as the value of n_s increases from $n_s = 1.5$ to $n_s = 5.0$, for all the corresponding values of b_s and a_s the volume fraction increases indicating a better quality. In addition, the sensitivity to b_s also decreases such that for $n_s = 5.0$ the volume fraction is practically independent of b_s. This perhaps is not surprising since larger n_s values cause a condensation of curvature very close to the edges and the remaining sections of profile away from the edges are essentially straight lines. Therefore, changing b_s does not significantly change the profile characteristics. For all values of $n_s \geq 1$ wider profiles generate beds with larger ϕ_s. The current results show that optimisation of the profile is highly successful and ϕ_s for $n_s = 5.0$, $a_s = 100D_{\text{sph}}$ and $b_s = 10D_{\text{sph}}$ approaches a value of $\phi_s = 0.58$ close to ϕ_s^c as identified in the earlier shear flow simulations (see Fig. 5). This is the largest ϕ_s one could expect from the spreading process without any subsequent compression.

For the particular powder considered here (with the specified material and morphology characteristics) a larger ϕ_s is obviously not anticipated and hence further optimisation is redundant. Nevertheless, since ϕ_s monotonically increased during the optimisation process (see Fig. 6a–e), a valid question is whether ϕ_s versus n_s curve has a plateau and one can choose an arbitrarily large n_s, or an optimum n_s value actually exists. It is important to note that as $n \to \infty$ the profile will approach a typical rectangular shape which as demonstrated in [1] significantly degrades the bed quality. Therefore, the existence of an optimum value for n_s is certain. To show that $n_s = 5.0$ is in fact that optimum value and generates the highest ϕ_s a series of the simulations with 3 other values of $n_s \in \{7.5, 10.0, 15.0\}$ are performed. The results are presented in Fig. 6f which proves that $n_s = 5.0$ (noting the resolution of the current parametric study) must be the optimum profile shape.

In this section, the profile with parameters $n_s = 5.0$, $a_s = 100D_{\text{sph}}$ and $b_s = 10D_{\text{sph}}$ is identified as the optimum profile. A value of $b_s = 10D_{\text{sph}}$ (=1 mm) may not be feasible to manufacture. However, noting the independence of ϕ_s from b_s in Fig. 6e, one can choose a larger value of b_s to manufacture a spreader with more realistic physical dimensions. For the rest of the paper a value of $b_s = 50D_{\text{sph}}$ is considered. In this section to control the cost of a large number of simulations only rod-shaped powder grains were considered. In the next section, the new designs will be applied to powder beds with realistic particle shapes to further demonstrate the effectiveness of the new designs compared to a roller.

4. Application to realistic particles

Particle shape is known to have a significant impact on the spreading process [1]. Therefore, in this section to show the effectiveness of the proposed design, first, realistic 3D models of PEEK particles are produced and a versatile minimum sphere packing algorithm is developed to generate a multi-sphere approximation (MSA) of the real PEEK particles. Then, the quality of a bed generated using the new design is compared to a roller-generated bed. It is also worth mentioning that impact milled PEEK particles are considered due to a generally superior roundedness and sphericity compared to the other production techniques [1]. In this section, an overview of the sphere packing approach will be provided and then the results will be discussed.

4.1. A new multi-sphere approximation strategy

The strategy used to produce a multi-sphere approximation of the real PEEK particles is based on a greedy heuristic (GH) algorithm recently proposed by Li et al. [28]. There are a few other techniques available in the literature, however, the GH algorithm proves to be very versatile and is capable of coping with highly irregular shapes automatically. The original algorithm has been modified and improved to generate MSAs suitable for large scale DEM simulations which will be discussed in this section.

To use a GH technique, first, a 3D representation of the particle's surface is required. To this end, an image processing algorithm is used to reconstruct 3D grain models from 2D Scanning Electron Microscope (SEM) images extracted from [29]. This has been done by adding depth to the image by first generating a "depth map" of the image followed by symmetric replication. The original SEM images are presented alongside the generated 3D stereo-lithography (STL) models in Fig. 7. It is possible to use more sophisticated techniques

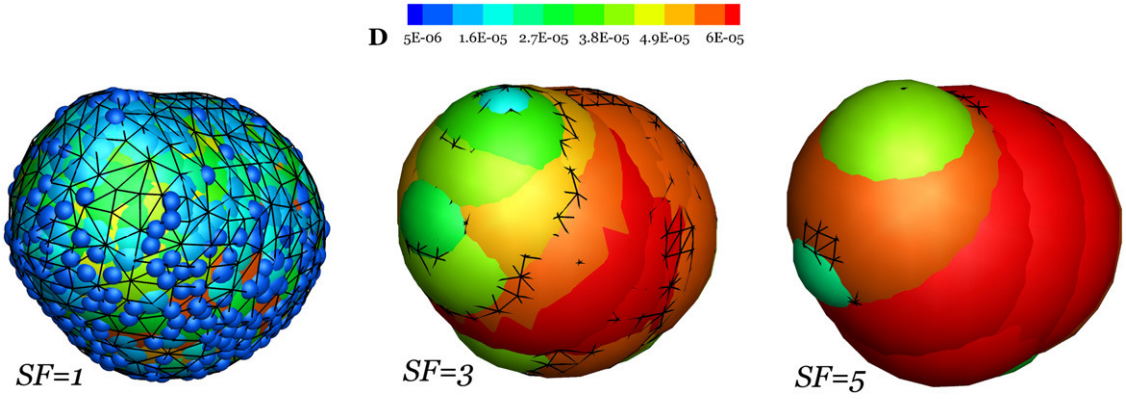

Fig. 9. Introduction of a smoothing factor into the new GH algorithm for controlling the number of spheres in the final MSA. The results with three different smoothing factors are presented. Spheres in the MSAs are coloured based on their diameters $D = 2R_{\text{ca}} + S_F w_{cell}$. From left to right $N_{\text{MSA}} = 732, 26, 11$ respectively.

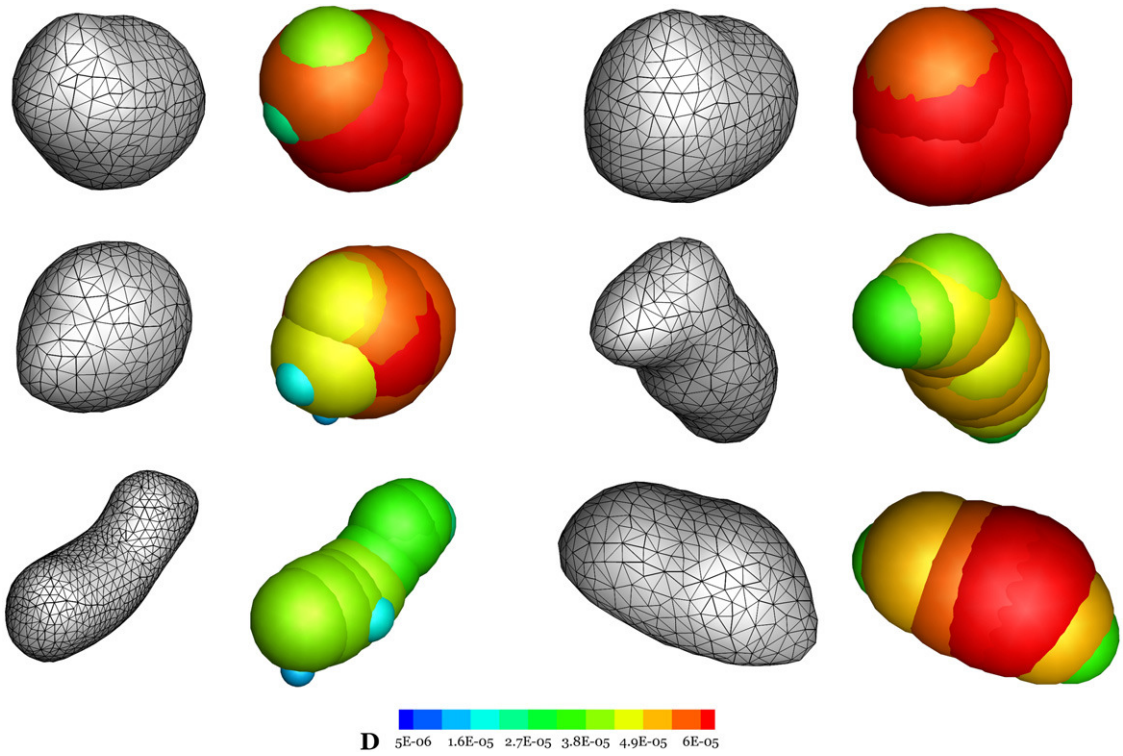

Fig. 10. MSAs generated for particle types $1\cdots6$ with $S_F = 5$. The spheres are presented with a diameter of $D = 2R_{ca} + S_F w_{cell}$.

to generate a 3D model of the grains (e.g. micro-tomography). However, it will be discussed later in this section that one can only hope to capture the general characteristic of the grains using a multi-sphere approach since retaining too much surface details will result in an MSA which comprises too many spheres to be feasibly included in a large scale DEM simulation.

The original GH algorithm starts by producing a discretization of the STL model. Li et al. [28] suggested to discretize the STL model using a collection of very small spheres (note that this is different from the final MSA). In this paper, a stair-step discretization is tested which has successfully been applied to other numerical schemes for fluid-particle interactions such as the fictitious domain method [30–33]. This technique has two significant advantages. Firstly, the calculation of volume, mass and moment of inertia will be trivial after a stair-step discretization since this will fully cover the entire volume compared to a discretization with spherical cells as suggested in Li et al. [28]. The volume and moment of inertia can be written as [32]

$$V_p = \sum_{\ell} \delta v_{\ell}, \tag{8}$$

$$\mathbf{I}_p = \sum_{\ell} \rho_p \left[(\mathbf{r}_{\ell} \cdot \mathbf{r}_{\ell}) \mathbf{I} - \mathbf{r}_{\ell} \otimes \mathbf{r}_{\ell} \right] \delta v_{\ell}. \tag{9}$$

The mass is then calculated simply by $m_p = \rho_p V_p$. In Eqs. (8) and (9), δv is the volume of the cell and $\mathbf{r}_{\ell}$ is the position vector of ℓth cell's centre and $\otimes$ is the outer product.

The second major advantage is that this could be generated much quicker than the Li et al.'s [28] discretization approach using spherical cells. One only needs to generate a bounding box for the STL then decide whether each cell falls within or outside of the STL by shooting a ray in any direction and calculating the number of intersection between the ray and the STL object. An odd number of intersections indicates that the cell is inside and even number of intersection indicates that the cell is outside the volume. The intersection between a collection of triangles and a line can be calculated very efficiently using the method of Moller and Trumbore [34] and is used here. The bounding box of each particle is discretized using 50 cells in each direction and the internal and surface cells are identified using the described method, see Fig. 8.

To show the accuracy of stair-step discretization, $\mathbf{I}_p$ calculated using Eq. (9) is compared to the values that are calculated using a standard Monte Carlo (MC) integration technique. The number of MC samples are increased step-by-step to 10^6 to ensure a relative accuracy of 10^{-3} for all the integrals. Note that one could use MC in conjunction with spherical cell discretization of [28] but the computational costs will be considerably higher. For both stair-step and MC methods one needs to decide whether the cell/sample is within the STL or not. Therefore, for example for the current calculation, the computational cost of the stair-step approach is only around 12% of the MC technique (1.25×10^5 decisions for stair-step method versus 10^6 for the MC). The V_p values from Eq. (8) are compared directly to the analytical volume of the STL object calculated using the divergence theorem by assuming an arbitrary (subject to $\nabla \cdot \mathbf{F} = 1$) vector field $\mathbf{F} = z\mathbf{e}_z$ to yield

$$V_p^{STL} = \sum_{\ell} z_{\ell}^c n_{\ell}^z \delta s_{\ell}, \tag{10}$$

where z_{ℓ}^c is the z-coordinate of a surface element ℓ, n_{ℓ}^z is the z-component of the element's outward unit normal and δs_{ℓ} is its area. The results of these calculations are summarised in Table 2. Evidently, all the relative errors are well below 1% confirming the high accuracy of the method which is achieved with little computational effort.

After identifying the N cells that discretize the STL, N_{bnd} boundary and N_{int} internal cells (see Fig. 8) are defined such that $N = N_{\text{int}} + N_{\text{bnd}}$. A set of N_{int} spheres are then defined on the location of N_{int} internal cells as candidates to be included in the final MSA. The distance between the centre of each candidate and N_{bnd} boundary

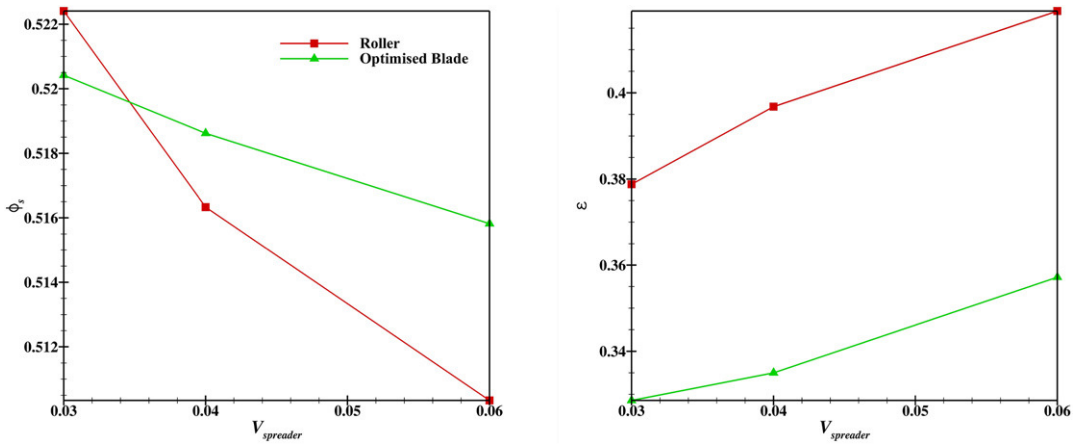

(a) Volume Fraction (b) Surface Roughness

Fig. 11. Comparison between a roller and the optimised blade type spreader (the legend applies to both figures). Clearly, the optimised blade type spreader produces a powder bed with volume fractions at least as good as the roller and surface roughness values are significantly better.

cells is calculated and the smallest one is chosen as the candidate's radius (R_{ca}). All the cells within each candidate are then identified and a binary mapping matrix ($M_{N\times N_{\text{int}}}$) is defined which takes a value of zero in its (i,j) location if the cell $i \in \{1\cdots N\}$ falls outside of the jth candidate $j \in \{1\cdots N_{\text{int}}\}$ and one otherwise. At each iteration, the candidate with the maximum number of constituent cells (i.e. column j where $\sum_{i=1}^{N} m_{ij}$ is maximum) is chosen as an accepted candidate. This column and the corresponding cells are then removed from the mapping matrix M until the matrix is reduced to $M_{0\times(N_{\text{int}}-N_{\text{MSA}})}$ where N_{MSA} is the number of spheres in the final MSA to be used for the DEM simulation.

The aforementioned algorithm is implemented and applied to the STL object of Type 1 particle (Fig. 7) to identify the optimum multi-sphere representation. The results are shown in Fig. 9, labelled $S_F = 1$. S_F is a smoothing factor which will be discussed in detail next. Real particles have a high level of surface roughness and the algorithm captures them with a resolution equivalent to the size of the smallest element. For example, the MSA generated with $S_F = 1$ in Fig. 9 is composed of 732 spheres which is too many for even a medium-scale (a few thousand particles) DEM simulation. To overcome this issue, a smoothing factor S_F is introduced and the radius of candidates are assumed to be $R_{\text{ca}} + S_F w_{cell}/2$, where w_{cell} is the width of the cells. Note that a minimum $S_F = 1$ is required to ensure all the cells are included in the final MSA. By introducing the smoothing factor S_F, number of spheres in the MSA is effectively controlled and is reduced from 732 to 26 and 11 for $S_F = 1$, 3 and 5 respectively. For the DEM simulations the radii could be scaled down to actual value R_{ca} if necessary.

A smoothing factor of 5 is used for all other particle types and the results are presented in Fig. 10. It is important to note that the spheres in Figs. 9 and 10 are presented with $D = 2R_{\text{ca}} + S_F w_{cell}$ to emphasise the effects of S_F. however, this has no impact on the calculation of V_p or $\mathbf{I}_p$ since the discretization of the bounding box is already culled using the STL object, therefore, no extra cells will be included.

4.2. Comparison of a roller with the optimised blade

In this section particles of Types 1–6 (see Fig. 10) are mixed with the same proportions to initialize the simulations. Three different translational velocities are considered for both the optimised blade and the roller. The results of this simulations are presented in Fig. 11.

Fig. 11a reveals that ϕ_s decreases by increasing the spreader translational velocity V^T_{spreader} which is the same trend reported in [1] for the simplified rod-shaped powder grains. More importantly, the optimised blade spreader generates a bed with volume fractions similar to that of the roller. In addition, the optimised blade is less sensitive to increasing the translational velocity V^T_{spreader} compared to the roller such that at higher velocities it outperforms the roller. This can be a significant advantage of the optimised blade type spreader and translates to faster production without a compromise in quality.

In Fig. 11b the value of surface roughness calculated as

$$\epsilon = \frac{\sqrt{\left\langle (h - \langle h\rangle)^2 \right\rangle}}{(\bar{V}_p)^{1/3}}, \tag{11}$$

is presented for all the simulations. Here, h is the height of the bed at various measurement points and averages are calculated using 5000 measurements over the surface of the bed. In addition, $\bar{V}_p$ is the average volume of particles of Type $1\cdots 6$. Clearly, the optimised blade performs much better compared to a roller by generating a smoother bed surface. The sensitivity of the roughness to increasing V^T_{spreader} however, is the same for both roller and the optimised blade.

5. Conclusion

In this paper it is first demonstrated that geometric optimisation of a blade type spreader can significantly improve the quality of a powder bed (a higher ϕ_s and lower ϵ) that is generated by spreading for Particle Bed Fusion (PBF) processes. A new class of spreading devices is proposed by assuming a super-elliptic edge profile with three different parameters controlling width, height and the overall shape of the profile. A set of 48 device-scale DEM simulations are performed and the optimum values for these parameters are identified. It is shown that this optimisation is highly effective and packings close to the critical volume fraction is achievable.

To fully demonstrate the effectiveness of the new design, it should be tested on realistic particle shapes. To this end, a new algorithm is developed to automatically generate multi-sphere approximations (MSA) from 3D STL models of the real powder grains used in the Particle Bed Fusion (PBF) process. The algorithm, is modified to generate

MSAs suitable for large-scale DEM simulations. The realistic particle shapes are then used to compare the quality of a powder bed prepared by a roller to that generated by the optimised blade.

It is shown that the optimised blade generates a bed with volume fractions very close to the roller. Interestingly, although the optimised blade generated a marginally lower volume fraction (0.4%) at the lowest spreader velocity $V^T_{\text{spreader}} = 0.03$, it is much less sensitive to increasing V^T_{spreader}, such that at higher tested velocities the volume fraction is actually greater (up to 2%) for the blade. This could be a significant advantage and means one can increase the velocity (translates to higher production rate) with limited impact on the quality. The surface roughness of the beds generated with both roller and the blade at different V^T_{spreader} are also compared and the new design outperforms the roller for all the tested V^T_{spreader} values.

Acknowledgments

The author gratefully acknowledges the use of ARCHER – The UK National Supercomputing Service (http://www.archer.ac.uk) – for conducting the simulations under the EPSRC's Resource Allocation Panel (RAP) Grant E504.

References

[1] S. Haeri, Y. Wang, O. Ghita, J. Sun, Discrete element simulation and experimental study of powder spreading process in additive manufacturing, Powder Technol. 306 (2017) 45–54.
[2] I. Gibson, D. Shi, Material properties and fabrication parameters in selective laser sintering process, RTejournal 3: Forum Rapid Technol., 1995.
[3] Y. Shi, Z. Li, H. Sun, S. Huang, F. Zeng, Effect of the properties of the polymer materials on the quality of selective laser sintering parts, IMechE J. 218 (2004) 247–253.
[4] R.D. Goodridge, K.W. Dalgarno, D.J. Wood, Indirect selective laser sintering of an apatite-mullite glass-ceramic for potential use in bone replacement applications., Proc. Inst. Mech. Eng. H 220 (2006) 57–68.
[5] L. Hao, M.M. Savalani, Y. Zhang, K.E. Tanner, R.A. Harris, Effects of material morphology and processing conditions on the characteristics of hydroxyapatite and high-density polyethylene biocomposites by selective laser sintering, J. Mater: Desi. Applic. 220 (2006) 125–137.
[6] S. Ziegelmeier, P. Christou, F. Wöllecke, C. Tuck, R. Goodridge, R. Hague, E. Krampe, E. Wintermantel, An experimental study into the effects of bulk and flow behaviour of laser sintering polymer powders on resulting part properties, J. Mater. Process. Technol. 215 (2015) 239–250.
[7] S. Berretta, O. Ghita, K. Evans, Morphology of polymeric powders in laser sintering (LS): from polyamide to new peek powders, Eur. Polym. J. 59 (2014) 218–229.
[8] P.A. Cundall, O.D.L. Strack, A discrete numerical model for granular assemblies, Geotechnique 29 (1979) 47–65.
[9] E. Onate, D.R.J. Owen, Particle-based Methods: Fundamentals and Applications, Computational Methods in Applied, Springer. 2011.
[10] T.I. Zohdi, Computation of the coupled thermo-optical scattering properties of random particulate systems, Comput. Methods Appl. Mech. Eng. 195 (2006) 5813–5830.
[11] T.I. Zohdi, Rapid simulation of laser processing of discrete particulate materials, Arch. Comput. Meth. Eng. 20 (2013) 309–325.
[12] T.I. Zohdi, Additive particle deposition and selective laser processing – a computational manufacturing framework, Comput. Mech. 54 (2014) 171–191.
[13] E. Parteli, T. Pöschel, Particle-based simulation of powder application in additive manufacturing, Powder Technol. 288 (2016) 96–102.
[14] Z. Xiang, M. Yin, Z. Deng, X. Mei, G. Yin, Simulation of forming process of powder bed for additive manufacturing, J. Manuf. Sci. Eng. 138 (2016) 081002.
[15] J.C. Steuben, A.P. Iliopoulos, J.G. Michopoulos, Discrete element modeling of particle-based additive manufacturing processes, Comput. Methods Appl. Mech. Eng. 305 (2016) 537–561.
[16] S. Plimpton, Fast parallel algorithms for short-range molecular dynamics, J. Comput. Phys. 117 (1995) 1–19.
[17] Y. Wang, D. Rouholamin, R. Davies, O. Ghita, Powder characteristics, microstructure and properties of graphite platelet reinforced poly ether ether ketone composites in high temperature laser sintering (HT-LS), Mater. Des. 88 (2015) 1310–1320.
[18] Y. Zhou, B. Wright, R. Yang, B. Xu, A. Yu, Rolling friction in the dynamic simulation of sandpile formation, Physica A 269 (1999) 536–553.
[19] J. Ai, J. Chen, J. Rotter, J. Ooi, Assessment of rolling resistance models in discrete element simulations, Powder Technol. 206 (2011) 269–282.
[20] C. Wensrich, A. Katterfeld, Rolling friction as a technique for modelling particle shape in DEM, Powder Technol. 217 (2012) 409–417.
[21] A. Di Renzo, F. Di Maio, Comparison of contact-force models for the simulation of collisions in DEM-based granular flow codes, Chem. Eng. Sci. 59 (2004) 525–541.
[22] A comprehensive review of the materials properties of VICTREX® PEEK™ high performance polymer, VICTREX, 2016.
[23] J. Shäfer, S. Dippel, D. Wolf, Force schemes in simulations of granular materials, J. Phys. I 6 (1996) 5–20.
[24] C.H. Rycroft, Voro++: a three-dimensional Voronoi cell library in C++, Chaos: Interdisciplinary J. Nonlinear Sci. 19 (2009) 041111.
[25] A.W. Lees, S.F. Edwards, The computer study of transport processes under extreme conditions, J. Phys. C 5 (1972) 1921–1928.
[26] S. Chialvo, J. Sun, S. Sundaresan, Bridging the rheology of granular flows in three regimes, Phys. Rev. E 85 (2012) 023305.
[27] C. Campbell, Elastic granular flows of ellipsoidal particles, Phys. Fluids 23 (2011) 013306.
[28] C.-Q. Li, W.-J. Xu, Q.-S. Meng, Multi-sphere approximation of real particles for DEM simulation based on a modified greedy heuristic algorithm, Powder Technol. 286 (2015) 478–487.
[29] S. Haeri, Dataset - discrete element simulation of powder spreading in additive manufacturing, 2016. http://dx.doi.org/10.15129/c5993a8f-812d-46cf-bef5-92e985d12446.
[30] S. Haeri, J. Shrimpton, On the application of immersed boundary, fictitious domain and body-conformal mesh methods to many particle multiphase flows, Int. J. Multiphase Flow 40 (2012) 38–55.
[31] S. Haeri, J.S. Shrimpton, A correlation for the calculation of the local Nusselt number around circular cylinders in the range $10 \leq Re \leq 250$ and $0.1 \leq Pr \leq 40$, Int. J. Heat Mass Transf. 59 (2013) 219–229.
[32] S. Haeri, J.S. Shrimpton, A new implicit fictitious domain method for the simulation of flow in complex geometries with heat transfer, J. Comput. Phys. 237 (2013) 21.45.
[33] S. Haeri, J.S. Shrimpton, Fully resolved simulation of particle deposition and heat transfer in a differentially heated cavity, Int. J. Heat Fluid Flow 50 (2014) 1–15.
[34] T. Moller, B. Trumbore, Fast, minimum storage ray-triangle intersection, J. Graphics Tools 2 (1997) 21–28.